A Vector Theory for Forward Propagation in a Structured Ionosphere with Surface Reflections

Charles Rino[1], **Charles Carrano,**[1]

[1]Institute for Scientific Research, Boston College, Newton, MA.

Key Points:

- In an earlier publication the scalar forward propagation equation was generalized to accommodate HF vector fields
- This companion publication incorporates reflections from a smoothly varying conducting boundary surface
- A comparison of collimated beam intensity with ray tracing shows a persistent but correctable bias

Corresponding author: Charles Rino, `crino@bc.edu`

Abstract

In a previous publication the forward propagation equation was generalized to accommodate vector propagation at HF frequencies. Solutions obtained with split-step integration were demonstrated for unbounded propagation and for a Chapman layer above a plane perfectly conducting boundary. This paper extends the solution to accommodate reflections from a smoothly varying boundary. A complete solution requires calculation of induced sources on the boundary surface. The fields from the induced sources, when combined with the incident field, satisfy the boundary conditions for the incident field vector components. Calculation of the induced sources can be incorporated in the split-step integration of the forward propagation equation. Alternatively, a variant of image theory reproduces the essential characteristics of the more computationally intensive boundary-integral methods. The paper concludes with ray-trace comparisons, which reveal a persistent but correctable bias.

1 Introduction

In a previous publication (C. Rino & Carrano, 2021), the forward propagation equation (FPE) was generalized to accommodate vector fields in the Earth's ionosphere at HF frequencies. Hereafter, we will refer to the generalized equation as the vector forward propagation equation (VFPE). The two-dimensional form of the VFPE confines propagation vector components to the yz plane. Although the field structure is invariant in planes displaced from the yz plane, the VFPE,

$$\frac{\partial \mathbf{E}(y,z)}{\partial z} = \Theta\mathbf{E}(y,z) + i\frac{k}{2}\Delta X(y,z)\overline{\chi}\mathbf{E}(y,z), \tag{1}$$

characterizes the progression of the three-dimensional electric field vector

$$\mathbf{E}(y,z) = E_x(y,z)\mathbf{u}_x + E_y(y,z)\mathbf{u}_y + E_z(y,z)\mathbf{u}_z. \tag{2}$$

The free-space propagation operation $\Theta\mathbf{E}(y,z)$ advances each vector component independently:

$$E_u(y, z+\Delta z) = \int \widehat{E}_u(\kappa_y, z)\exp\{ikg(\kappa)\Delta z\}\exp\{iy\kappa_y\}\frac{d\kappa_y}{2\pi} \tag{3}$$

where

$$\widehat{E}_u(\kappa_y, z) = \int E_u(y,z)\exp\{-iy\kappa_y\}dy, \tag{4}$$

with $u = x$, y, or z. The two-dimensional propagation vector, $\mathbf{k}$, is defined by the spatial wavenumber, κ_y, and the constant magnitude, $k = 2\pi f/c$, where f denotes frequency and c is the vacuum velocity of light:

$$\mathbf{k} = [0, \kappa_y/k, g(\kappa_y)] \tag{5}$$

$$g(\kappa_y) = \sqrt{1-(\kappa_y/k)^2} \tag{6}$$

The product $\Delta X(y,z)\overline{\chi}$ represents the susceptibility tensor[1], which is defined in the appendix of (C. Rino & Carrano, 2021). Structure variation is confined to the scalar multiplier $X(y,z)$. The complete susceptibility tensor characterizes the local interaction of the vector field in response to the ionosphere with a uniform background magnetic field. The direction of the magnetic field determines the components of the 3×3 matrix, $\overline{\chi}$, which has 3 distinct eigenvectors. All three eigenvectors are used in the split-step integration of the VFPE as described in (C. Rino & Carrano, 2021).

[1] The dielectric tensor is defined as $\overline{\epsilon} = \overline{I} + \Delta X\overline{\chi}$.

Vector fields are initiated in the xy plane at $z = 0$ by specifying $E_x(y, 0)$ and $E_y(y, 0)$ normalized to unit total intensity. The $E_z(y, 0)$ component is set to zero but could be specified if it were meaningful to do so. Either linear or circular polarization can be used.

Chapter 4.8 in (Budden, 1985) discusses energy conservation. For propagation oblique to the magnetic field direction interaction with the ionosphere will generate a finite E_z field component. When this happens energy flow does not follow the direction of propagation. Energy is conserved, although energy stored in the magnetic field can reduce total field intensity carried by the E_x and E_y components. In the simulations energy is absorbed at the upper boundary to mimic propagation outside the measurement space.

Specification of the incident field, the magnetic field vector, and $X(y, z)$ completely define field realizations. The propagation problems of primary interest involve a radially varying electron density with embedded structure. Time-harmonic field solutions are formally snapshots that remain invariant over the time a waveform comprised of a band of frequencies traverses the realization space. The frequency dependence of the field components imposes a group-velocity constraint. Determining paths that wave packets can follow is a secondary computation most often guided by ray-tracing. We expect an upward propagating beam, upon interacting with the ionosphere, to split into ordinary (O) and extraordinary (X) modes with complementary polarizations that provide a basis for mode separation.

Real-world applications invariably involve surface reflections. The same theory that produced the first-order VFPE differential equation can be adapted to incorporate surface reflections. The solution involves induced sources on the surface that function in the same way as the induced ionospheric sources. Calculating induces sources on the boundary requires the separate solution of boundary integral equations (BIEs). Once the induced sources are calculated, the total field above the surface can be constructed. Upon introducing the forward approximation, the BIE solution and the field reconstruction can be incorporated in the split-step integration of the VFPE. However, the computations require sub-wavelength sampling and careful accommodation of the Green-function singularity on the surface.

Surface reflections have been accommodated in scalar FPE simulations by using a variant of image theory, which is referred to as *shift mapping* (Donohue & Kuttler, 2000). The shift mapping operation involves an adjustment of the computation reference to the next stair-step surface height. The method is most often used in conjunction with impedance boundary conditions. FPE solutions in unbounded media typically use propagation steps exceeding hundreds of wavelengths. However, to minimize the effects of the step approximation discontinuities, sampling at near-wavelength must be used. A demonstration of split-step VFPE integration that fully accommodates a perfectly conducting spherical-earth boundary is demonstrated, although the image method is satisfactory for most applications.

2 Surface Reflections

Boundary surfaces delineate discontinuous changes in the propagation medium. Induced surface currents must flow on the boundaries to support the discontinuous field changes. Although a discontinuous boundary is an idealization, experience has shown that fields above an ideal boundary surface capture the critical characteristics of scattered or reflected fields from real surfaces.

2.1 Boundary Integral Methods

Two-dimensional boundary surfaces intersect the yz plane along a contour. The simplest contour is defined by a single-valued function $f(z)$ such that $y = f(z)$ defines the surface height at z. Let $E_{\|}(y,z)$ denote the surface-parallel x or z field components, which are treated identically. The $E_y(y,z)$ component is perpendicular to the surface. A standard text-book exercise will show that total fields above the surface ($y > f(z)$) are characterized by the following equations:

$$E_{\|}(y,z) = E_{\|}^{0}(y,z) - \frac{i}{4}\int_0^\infty H_0^0(k\rho(y,f(z');z,z'))S_{\|}(z')dz' \tag{7}$$

$$E_y(y,z) = E_y^i(y,z) + \frac{i}{4}\int_0^\infty \frac{\partial H_0^{(1)}(k\rho)(y,f(z');z,z')}{\partial N'}S_y(z')dz' \tag{8}$$

where $H_0^{(1)}(z)$ is the first-kind Hankel function of order 0. The theory can also be formulated with a second-kind Hankel function, which reverses the sign of the radial variable. The free propagation of the incident fields initiated at $z = 0$ are denoted by the 0 superscript. Detailed developments can be found in Chapter 3 in (Morita et al., 1990) or Appendix A.5 in (C. L. Rino, 2011).

The boundary-integral equations (BIEs) that define the induced source functions, are obtained by calculating the field and its normal derivative on the surface. The equations are written here as

$$\frac{1}{2}\frac{\partial E_{\|}(f(z),z)}{\partial N} = \frac{\partial E_{\|}(f(z),z)}{\partial N}^0 - \frac{i}{4}\int_{z_0}^\infty \frac{\partial H_0^{(1)}(k\rho(f(z),f(z');z,z')}{\partial N}\frac{\partial E_{\|}(f(z'),z')}{\partial N}dz' \tag{9}$$

$$\frac{1}{2}E_y(f(z),z) = E_y(f(z),z)^0 + \frac{i}{4}\int_{z_0}^\infty \frac{\partial H_0^{(1)}(k\rho(f(z),f(z');z,z')}{\partial N'}E_p(f(z'),z')dz'. \tag{10}$$

where

$$S_{\|}(z) = \partial E_{\|}(f(z),z)/\partial N \tag{11}$$

$$S_y(z) = E_y(f(z),z) \tag{12}$$

The normal derivative is defined as

$$\frac{\partial}{\partial N} = \frac{\partial}{\partial y} + \frac{\partial f}{\partial z}\frac{\partial}{\partial z}, \tag{13}$$

and

$$\Delta\rho(y,y';z,z') = \sqrt{(y-y')^2 - (z-z')^2} \tag{14}$$

is the distance between (y,z) and (y',z').

In (C. L. Rino & Ngo, 1997) it was shown that upon truncating the integrals in (9) and (10) at z, which imposes the forward approximation, the following recursive solution can be obtained:

$$S_{\|,y}(z_{n+1}) = \left(S_{\|,y}^i(z_{n+1}) \mp \Lambda_{n+1,n}S_{\|,y}(z_n)\right)/(1/2 \pm \Lambda_{n+1,n+1}) \tag{15}$$

where

$$\Lambda_{n,m} = \int_{-\Delta z/2}^{\Delta z/2} \frac{kH_1^{(1)}(k\Delta\rho(f(z_m),f(z'-z_n);z_m,z'-z_n))}{\Delta\rho(f(z_m),f(z'-z_n);z_m,z'-z_n))}\varsigma(z_m,z')dz' \tag{16}$$

$$\varsigma(z_m,z') = (f(z_m)-y') - \frac{\partial f_z(z_m)}{\partial z}(z_m - z') \tag{17}$$

$$\Lambda_{n,n} = \frac{\partial^2 f(z_n)}{\partial^2 z}\Big/\left(1+\frac{\partial^2 f(z_n)}{\partial^2 z}\right) \tag{18}$$

The upper sign is used for the parallel (Dirichlet) induced source. The lower sign is used for the perpendicular (Neuman) induced source. The total field is advanced from z_n to z_{n+1} by evaluating the forward contributions to the fields at z_{n+1}:

$$\begin{aligned} E_{\parallel}(y, z_{n+1}) &= E^0_{\parallel}(y, z_{n+1}) \\ &\quad - \frac{i}{4} \int_{z_0}^{z_{n+1}} H_0^{(1)}(k\rho(y, f(z'); z_{n+\Delta z}, z')) S_{\parallel}(z') dz' \end{aligned} \tag{19}$$

$$\begin{aligned} E_y(y, z_{n+1}) &= E^0_y(y, z_{n+1}) \\ &\quad + \frac{i}{4} \int_{z_0}^{z_{n+1}} \frac{\partial H_0^{(1)}(k\rho(y, f(z'); z_{n+\Delta z}, z'))}{\partial N'} S_p(z') dz' \end{aligned} \tag{20}$$

The integrals in (19) and (20) have contributions from the induced source term at z_n and a singular contribution from the induced source at z_{n+1}. This is shown schematically in Figure 1. The blue arrows represent the contributions from induced sources. The orange arrow represents the freely propagating field components. To complete the recursion it is necessary to calculate the total field on the surface. For parallel components the total field on the surface is zero, whereby computing the field on the surface and its cancellation by the induced source is unnecessary. For the perpendicular component the surface field is finite, whereby computing source term is necessary and demanding because of the Green function singularity on the surface.

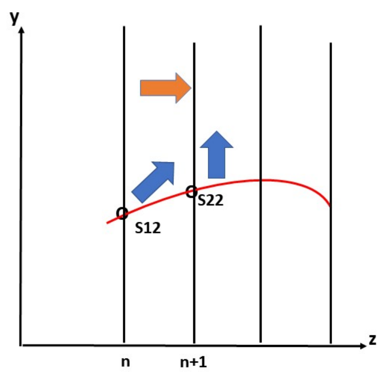

Figure 1. Schematic diagram of total field contributions for calculating the field at z_{n+1} from the known field and its sources at z_n.

If the total fields and their source functions are known at $z = z_n$, the source functions can be advanced to $z = z_{n+1}$ by using (15). The total field can then be updated by evaluating (19) and (20). This was demonstrated in (C. L. Rino & Ngo, 1997) with both sinusoidal and stochastic surface variations at 1 GHz, although it was stated erroneously that the source at z_{n+1} was unnecessary. The calculation is repeated here for a plane conducting surface at 10 MHz. Figure 2 shows the intensities of the perpendicular (upper frame) and parallel (lower frame) field components initiated by an E_y field with the intensity and phase variation adjusted to launch a downward propagating beam. The lower frame, which was initiated with an identical excitation field, could represent either E_x or E_z. The surface reflection calculations here were performed for propagation in a vacuum. The sampling was adjusted to conserve the reflected field total intensity.

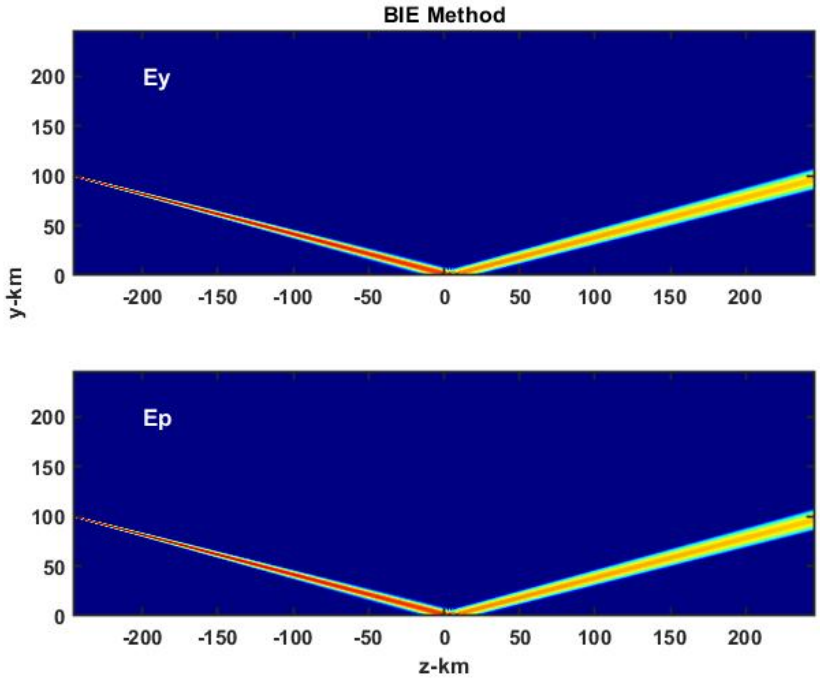

Figure 2. Field Intensity in dB units for perpendicular (upper frame) and parallel (lower frame) surface reflections from downward propagating 10 MHz beam.

Note that the scalar field component intensities are independent and identical above the surface. Impedance boundary conditions would couple the equations, whereby the field component intensities would differ, reflecting the surface conditions. Either way, the supporting sources and fields on the surface differ significantly. For now, only perfect conductivity will be used. It has already been noted that for the parallel component the total field on the surface is zero, which requires the incident field to cancel the source function field. For the perpendicular component the field on the surface is large. Consequently, managing the singular contribution from Green function is more demanding. Further insight can be gleaned from the method of images as discussed in the next section.

2.2 Image Theory Methods

It is well known that reflections from a perfectly conducting plane can be calculated by removing the surface and placing a positive (Neuman) or negative (Dirichlet) image of the source below the surface. This is achieved formally by propagating the field with only Fourier cosine (Neuman) or sine (Dirichlet) components. The field where the original conducting surface existed is zero, which is automatic for an antisymmetric reflection. For forward propagation applications the image field is constructed at each propagation step.

Applying the method of images requires only manipulation of Fourier transforms, whereby representative data spaces are readily accommodated. Figure 3 shows a computation for a 500-by-3000 km data space, with 32768 y samples and 5000 VFPE steps, which corresponds to 20 wavelengths per sample. The parallel component, which would apply to E_x or E_z components, was computed with the Fourier sine series. The perpendicular E_y field component was computed using the Fourier cosine series. The E_y field shows spurious surface reflections, which can be explained by the fact that the cosine basis functions are finite at the surface. The fields being constructed are small near the surface, whereby propagation-step errors are amplified. However, for perfectly conducting surfaces, the fact that the scalar complex amplitudes of the two components are identical, can be exploited by using sine series, which is less sensitive to surface-field errors, for both components.

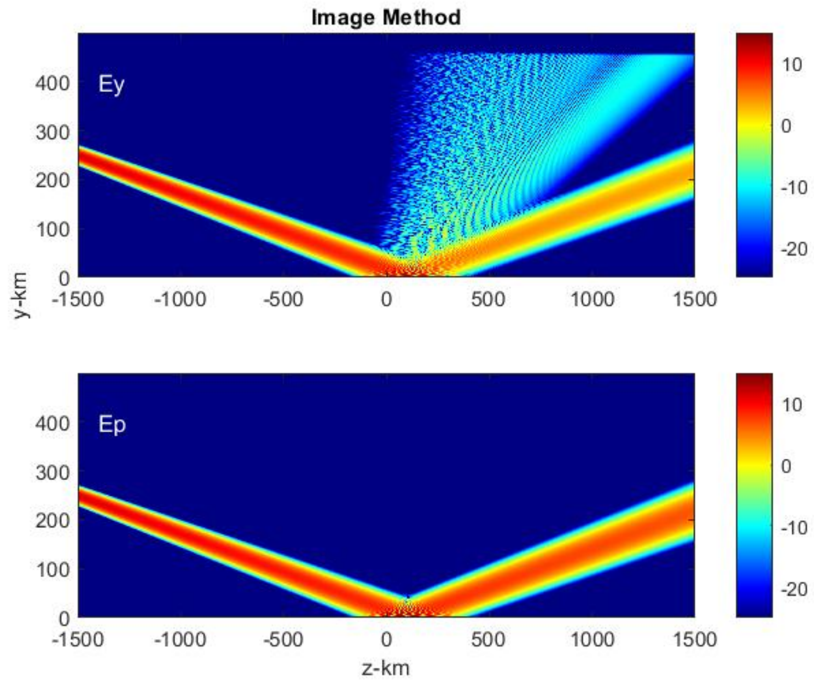

Figure 3. Field intensity in dB units for symmetric (upper frame) and antisymmetric (lower frame) reflections of 10 MHz beam from a perfectly conducting plane surface.

In a later paper (C. L. Rino & Kruger, 2001), which provided the framework for developing the VFPE, a variant of the recursion calculation was used. The induced surface currents were computed using several integration steps. The finer propagation step sampling improves the calculation of the surface reflection within the coarser propagation step typically used for incorporating the structure in the propagation medium.

A much simpler shift-mapping method was introduced by (Kuttler & Dockery, 1991) and (Dockery & Kuttler, 1996). The only change needed to accommodate a non-planar surface is the addition of a phase shift that translates the reference to the surface:

$$\exp\{ikg(\kappa_y)\Delta z\}\exp\{i\kappa_y(f(z_n)-f(z_{n-1}))\}. \tag{21}$$

It was shown in both (C. L. Rino & Ngo, 1997) and (C. L. Rino & Kruger, 2001) that BIE and shift-map solutions agreed very well. However, the comparisons used sub-wavelength propagation-step sampling for both the BIE and shift-map results. For accommodating smooth surface reflections in VFPE split-step solutions we find that near-wavelength sampling provides good results as indicated by total field intensity conservation through the surface reflection.

3 VFPE and Ray Theory

Solutions to the wave equation and the VFPE are constrained only by the susceptibility tensor, $\Delta X(y,z)\overline{\chi}$. In particular, there is no prior identification of characteristic modes. In (C. Rino & Carrano, 2021) we showed that in a medium with gradients confined to the propagation direction, solutions to the two-dimensional VFPE can be constructed from superpositions of O and X characteristic modes. The characteristic modes are defined by the Appleton-Hartree equations as summarized in the (C. Rino & Carrano, 2021) Appendix. [2] The more general identification of characteristic modes in inhomogeneous media comes from ray theory, which starts with the assumption that the field can be approximated locally as

$$\mathbf{E}(y,z) = \mathbf{E}_0(y,z)\exp\{i\vartheta(y,z)\}, \tag{22}$$

where $\mathbf{E}_0(y,z)$ varies slowly compared to the eikonal, $\vartheta(y,z)$.

Surfaces of constant $\vartheta(y,z)$ identify wave fronts. Rays are paths normal to the wavefronts. Rays are identified by a formal minimization procedure that constructs the shortest paths connecting two points in the medium. The connecting rays are defined by their direction angles at the point of initiation. Introducing the susceptibility matrix leads to a quadratic equation whose roots identify the characteristic modes being traced.[3] To the extent that $\vartheta = \mathbf{r}\cdot\mathbf{n}$ along the ray, the magnitude of $\mathbf{n}$ defines the local refractive index. Ray theory shows as well that the fields associated with the characteristic modes have orthogonal elliptical polarizations.

Regarding comparisons between FPE realizations and ray theory, it has been observed that VFPE field structures respond to gradients in the propagation medium with local propagation direction changes. Spatial wavenumber intensity peaks identify local propagation directions. Lines connecting the tangent vectors are effectively ray paths (Carrano et al., 2020). To associate ray paths with characteristic modes the VFPE E_x and E_y field components are combined to extract orthogonal elliptically polarized field components. Formally,

$$E_M = E_x \pm S\cdot E_y. \tag{23}$$

where $S = i$ or $= 1$ for linear or circular incident polarization, respectively. Anticipating the association with characteristic modes, we let $M = O$ and $M = X$ as tentative mode associations.

Figures 4 and 5 summarize extensions of the Chapman layer result introduced in (C. Rino & Carrano, 2021) Figures 9 and 10. [4] The upper frames in Figures 4 and 5 show the intensities of the candidate mode fields constructed as described above. The lower frames show the corresponding spectral-domain intensities plotted against normalized spatial wavenumber. The $\pm 1\ \kappa_y/k$ range includes all propagating waves. The peak intensities of the extracted modes and their spectral decompositions can be associated with ray positions and directions, respectively. Discontinuous direction reversals identify the locations of surface reflections. The extracted peak intensities and directions are shown in Figure 6.

[2] In the VFPE coordinate system $\mathbf{u}_B = [0, \sin(\phi_B), \cos(\phi_B)]$. For a horizontal B field$\phi_B = \pi/2$.

[3] See for example Equation (16) in (Coleman, 2008).

[4] The Chapman layer is defined as

$$Ne = Nm\exp((1-(h-Hm)/H0 - \exp(-(h-Hm)/H0)/2)) \tag{24}$$

with $Nm = 10^{12}\ m^{-3}$, $Hm = 350$ km, and $H0 = 50$ km. Height is measured radially from the spherical-earth surface intercept.

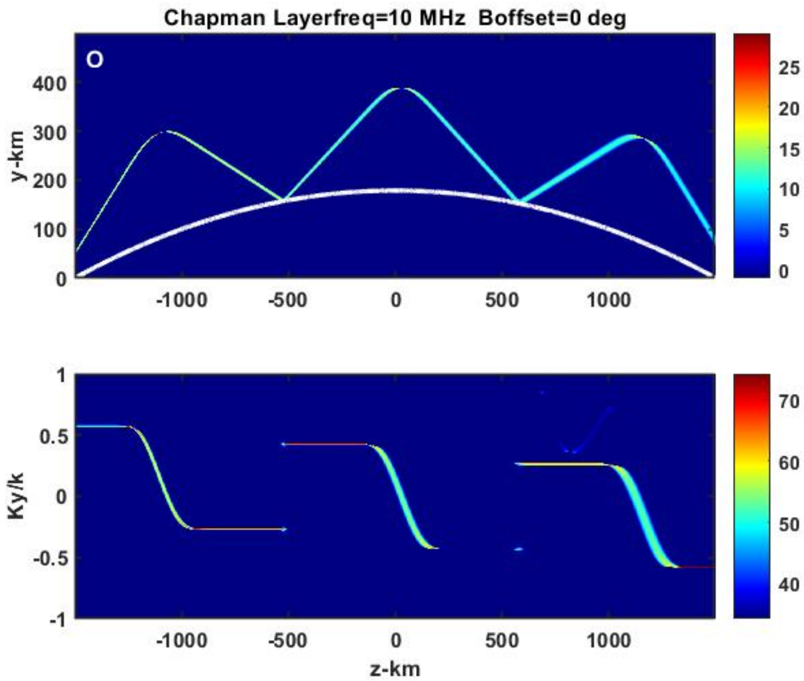

Figure 4. The upper frame shows the dB intensity of the elliptically polarized beam response identified as the O mode. The lower frame is the corresponding spectral intensity normalized to the wave vector magnitude in dB units.

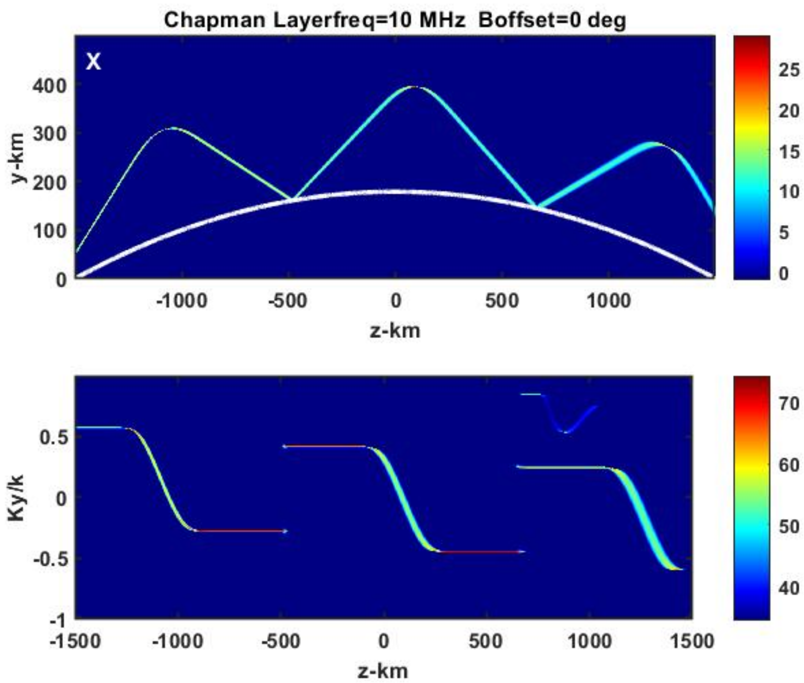

Figure 5. The upper frame is the dB intensity opposite elliptically polarized beam response identified as the X mode. The lower frame is the corresponding spectral intensity normalized to the wave vector magnitude in dB units.

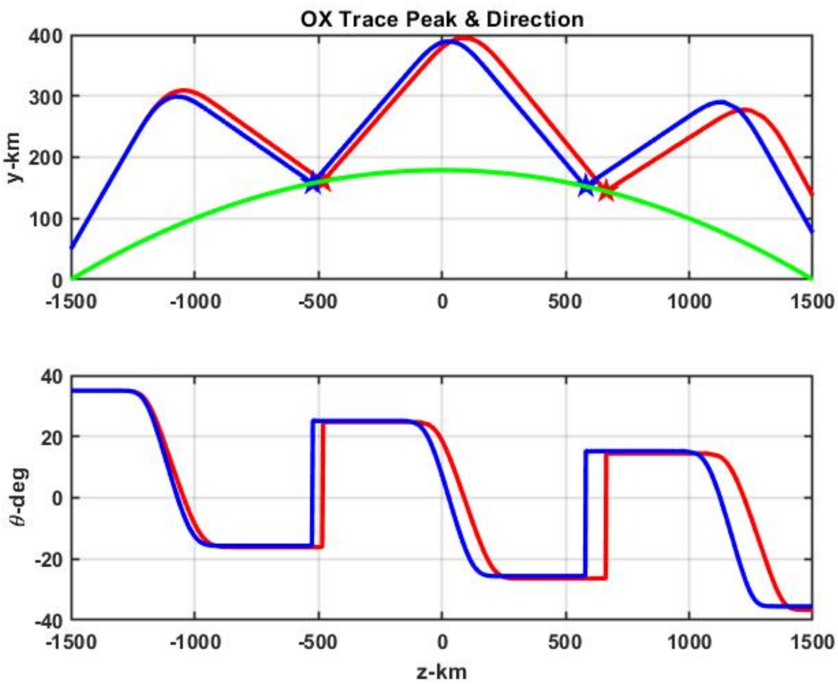

Figure 6. The upper frame shows the O mode (red) and X mode (blue) peaks. The lower frame shows the corresponding spectral-domain peaks plotted against propagation direction. The pentagrams mark the discontinuous spectral-domain changes in propagation direction.

Figure 7 shows a comparison of the VFPE O and X mode traces from the upper frame of Figure 6 with ray-trace calculations from the PHaRLAP code. [5] The comparison shows that the VFPE solutions (red) are not rotated by the ionosphere as strongly as the ray-trace solutions (blue). Considerable care was taken to ensure that the geometric translations and the parameter specifications are consistent. We believe the resulting bias is real and can be attributed to an approximation made in deriving the VFPE as follows.

The approximation used to evaluate Equation (24) in (C. Rino & Carrano, 2021) is reproduced here as

$$k^2 \int\int \mathbf{S}(\overrightarrow{\eta}')\mathbf{G}(\overrightarrow{\eta}, \overrightarrow{\eta}')d\overrightarrow{\eta}' \simeq i\frac{k}{2}\mathbf{S}(\overrightarrow{\eta}), \tag{25}$$

where $\mathbf{S}(\overrightarrow{\eta}) = \Delta X(\overrightarrow{\eta}, z)\overline{\chi}\mathbf{E}(\overrightarrow{\eta}, z)$

$$\mathbf{G}(\mathbf{r}, \mathbf{r}') = [\mathbf{I} + (1/k)^2 \nabla\nabla] G\left|\mathbf{r} - \mathbf{r}'\right|) \tag{26}$$

is the dyadic Green function, and

$$G\left|\mathbf{r} - \mathbf{r}'\right|) = \frac{\exp\{ik\left|\mathbf{r} - \mathbf{r}'\right|\}}{4\pi\left|\mathbf{r} - \mathbf{r}'\right|} \tag{27}$$

is the scalar Green function. The approximation follows from the observation that if $\mathbf{S}(\overrightarrow{\eta}')$ is constant over the defining range of the Green function, the integration of the dyadic

[5] PHaRLAP is a 3-D magnetoionic Hamiltonian ray tracing engine developed by the Australian Defence Science and Technology Organisation (DSTO) (Cervera & Harris, 2014).

Green function can be evaluated as

$$\int\int \mathbf{G}(|\overrightarrow{\eta} - \overrightarrow{\eta}'|)d\overrightarrow{\eta}' = i/(2k)\,. \tag{28}$$

Neglecting the variation of $\mathbf{S}(\overrightarrow{\eta}')$ and applying (28) produces the VFPE induced-source contribution.

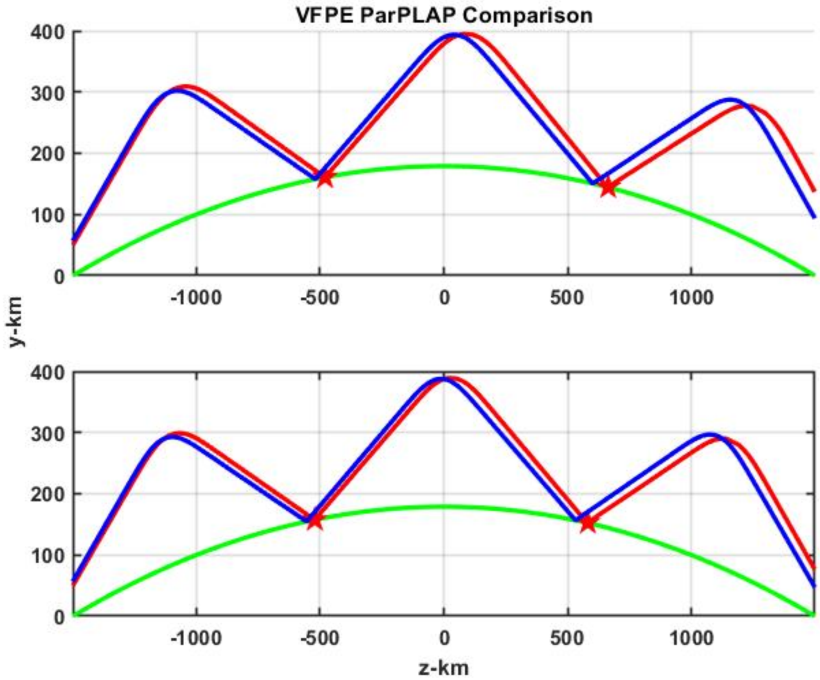

Figure 7. The upper frame compares the O-mode trace shown in the upper frame of Figure 23 (red) with the O-mode trace predicted by the PHaRLAP code (blue). The lower frame shows the same comparison for the X-mode trace and the PHaRLAP code prediction.

Validating the approximation is difficult. However, if the variable component, $\Delta X(\overrightarrow{\eta})$, is the leading term in a perturbation series, the corrected form of (25) would have $\Delta X(\overrightarrow{\eta})+ \Delta X(\overrightarrow{\eta})^2/2$. Although the correction is purely conjectural, it is very effective. Figure 8 reproduces the comparison in Figure 7 with the corrected VFPE result. The PHaRLAP raytrace and the VFPE results are indistinguishable on the scale plotted. The same agreement is found when the magnetic field direction is varied from the horizontal direction for the example shown.

To demonstrate that a disparity between ray-trace and VFPE results might be expected, consider the simplified form of the Haselgrove equations when $B = 0$. Equation (39) in (Coleman, 2008) is the $B = 0$ limiting form, which is rewritten here as

$$n\frac{d^2\mathbf{r}}{ds^2} + \frac{dn}{ds}\frac{d\mathbf{r}}{ds} = \nabla n, \tag{29}$$

where s represents distance along the ray, and n is a scalar refractive index. The result is well known. Equation (3.2.1.2) in (Born & Wolf, 1999) follows a direct derivation from the scalar wave equation. From (29) we see that an incremental ray-trace step starts with the gradient of the refractive index, which is functionally similar to the phase perturbation that initiates an FPE integration step. However, the FPE propagation step im-

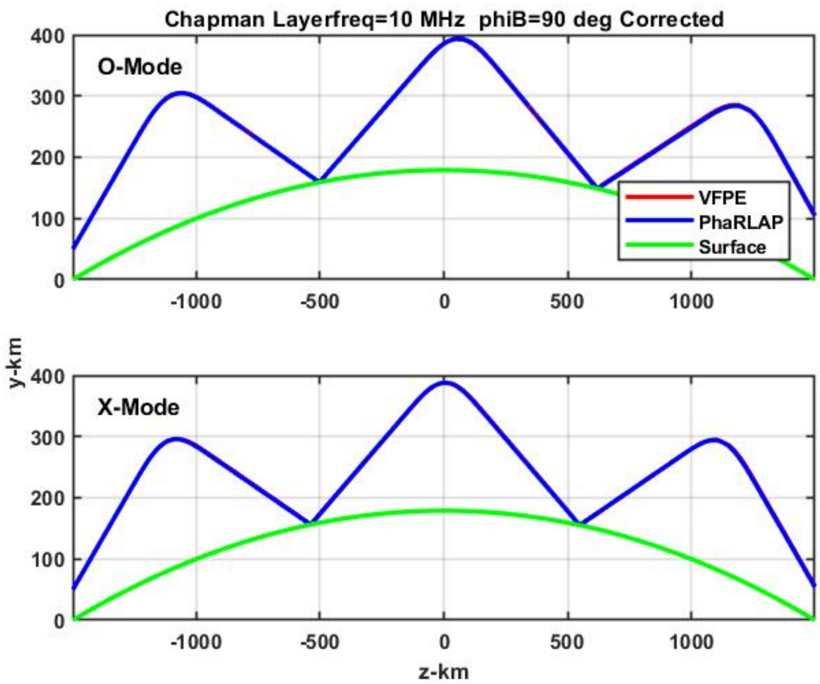

Figure 8. Recalculation of VFPE result shown in Figure 7 with VFPE correction.

poses no further direction change. In (29) the curvature term, $d^2\mathbf{r}/ds^2$, imposes an additional ray direction change from the direction of the refractive index gradient. Evidently, the quadratic correction provides the additional VFPE directional change needed to match the ray trace. For the scalar ionosphere, $n = \sqrt{1-(\omega/\omega_p)^2}$. As a qualitative extension of the scalar ray theory, the Appleton-Hartree O and X refractive indices can be substituted for n in (29). Although the modified scalar theory is not accurate, it has been used for interpreting HF diagnostic measurements (Tsai et al., 2010). As a general rule, ray theory redirects a wavefront more strongly than an uncorrected separation of propagation and media interaction.

Although unrelated to ionospheric redirection of rays, we note that surface reflections are accommodated by truncating rays that intercept the surface and initiating a new ray in the direction reflected about the known surface normal. The VFPE reflection involves a translation that takes place over several kilometers. The direction changes of the corrected VFPE rays coincide with the ray intercepts.

4 Summary and Future Applications

Our previous paper (C. Rino & Carrano, 2021) extended the scalar FPE to accommodate polarizations effects, which are important for HF propagation. This paper further extends the development to accommodate boundary reflections. The formalism is fully three-dimensional. However, computational requirements are reduced significantly for two-dimensional propagation and a spherical-earth perfectly conducting boundary surface. Near-wavelength sampling (2 wavelengths per sample) in the propagation direction is necessary to reproduce specular surface reflections accurately. Critical sampling (2 samples per wavelength) is a guide for FPE applications in general. We believe the sampling used is adequate to accommodate stochastic structure, which will be explored in future applications.

With regard to ray tracing, we emphasized that both the wave equation and the VFPE approximation are constrained only by the susceptibility matrix. Their is no prior identification of characteristics modes. We identified characteristic-mode candidates in much the same way that they would be identified with real field measurements, namely by extracting orthogonal field polarization components. We initiated the calculations with contrived narrow beams concentrated in both direction and position. We showed that the direction and position of the polarization-dependent fields could be measured through ionospheric reflections and surface reflections.

The measured rays were compared to predictions using the PHaRLAP code. We found that the PHaRLAP rays were consistently refracted more than the VFPE rays. We attributed this bias to a VFPE approximation, which incorporates the media interaction as a phase perturbation. We found that a quadratic correction eliminated the bias, although we have no rigorous derivation of the correction term. However, *any* application of the scalar FPE or parabolic wave equation is subject to the bias, which suggests replacing ΔX with $\Delta X + \Delta X^2/2$ whenever applications are used.

The development of a vector extension of scalar VFPE was undertaken to generate simulations for improved HF direction finding, communications, and diagnostics in highly disturbed environments. Scalar simulations have been very effective for designing robust GNSS systems (Xu et al., 2019). Simplified scalar FPE solutions underly the simulations used for the evaluations. The VFPE is the starting point for similar HF system evaluations.

Acknowledgments

This work was supported by U. S. Air Force Office of Scientific Research under Contract FA8650-20-C-1950. All the results shown in the paper can be reproduced by implementing the VFPE as summarized in algorithmic form. The HF propagation toolbox, PHaRLAP, can be downloaded from https://www.dst.defence.gov.au/.

References

Born, M., & Wolf, E. (1999). *Principles of optics.* Cambridge University Press.

Budden, K. G. (1985). *The propagation of radio waves.* Cambridge University Press, Cambridge.

Carrano, C. S., Retterer, J. M., Groves, K. M., Crowley, G., Duly, T. M., & Hunton, D. E. (2020). Wave-optics analysis of hf propagation through traveling ionospheric disturbances and developing plasma bubbles. *URSI GASS 2020, Rome, Italy, 29 August - 5 September 2020*.

Cervera, M. A., & Harris, T. J. (2014). Modeling ionospheric disturbance features in quasi-vertically incident ionograms using 3-d magnetoionic ray tracing and atmospheric gravity waves. *J. Geophys. Res. Space Physics*(119), 431440. (doi:10.1002/2013JA019247)

Coleman, C. (2008). Ionospheric ray tracing equations and their solution. *The Radio Science Bulletin*, *39*.

Dockery, G. D., & Kuttler, J. R. (1996). An improved impedance boundary algorithm for Fourier split-step solutions of the parabolic wave equation. *IEEE Trans. Antennas Propagat.*, *44*, 1592-1599.

Donohue, D. J., & Kuttler, J. R. (2000). Propagation modeling over terrain using the parabolic wave equation. *IEEE Transactions on Antennas and Propagation*, *48*.

Kuttler, J. R., & Dockery, G. D. (1991). Theoretical description of the parabolic approximation/Fourier split-step method of representing electromagnetic propagation in the troposphere. *Radio Science*, *26*, 381-393.

Morita, N., Dumagai, N., & Mautz, J. R. (1990). *Integral equation methods for electromagnetics.* Artech House, Inc.

Rino, C., & Carrano, C. (2021). A vector theory for forward propagation in a structured ionosphere. *Journal of Atmospheric and Terrestrial Physics*. (doi.org/10.1016/j.jastp.2021.105558)

Rino, C. L. (2011). *The theory of scinillation with applications in remote sensing.* Wiley.

Rino, C. L., & Kruger, V. R. (2001). A comparison of forward boundary integral and parabolic wave equation propagation models. *IEEE Trans Prop. Antennas*, *49*.

Rino, C. L., & Ngo, H. D. (1997). Forward propagation in a half-space with an irregular boundary. *IEEE Trans Prop. Antennas*, *45*.

Tsai, L.-C., Liu, C. H., & Huang, J. Y. (2010). Three-dimensional ray tracing on a phenomenological model. *Radio Science*, *45*. (doi:10.1029/2010RS004359)

Xu, D., Morton, Y., & Yang, R. (2019). A comparative performance analysis of advanced gnss carrier tracking algorithms during strong equatorial ionospheric scintillation. *IEEE Transactions on Aerospace Electronic Systems*. (doi:)